A&A 487, 805–813 (2008)
DOI: 10.1051/0004-6361:20079272

Astronomy & Astrophysics

Radiative transfer in cylindrical threads with incident radiation

V. 2D transfer with 3D velocity fields

P. Gouttebroze

Institut d'Astrophysique Spatiale, Univ. Paris XI/CNRS, Bât. 121, 91405 Orsay Cedex, France
e-mail: pierre.gouttebroze@ias.u-psud.fr

Received 19 December 2007 / Accepted 28 April 2008

ABSTRACT

Context. Time-resolved observations of loops embedded in the solar corona show the existence of motions of matter inside these structures, as well as the global motions of these objects themselves.
Aims. We have developed a modeling tool for cylindrical objects inside the solar corona, including 2-dimensional (azimuth-dependent) radiative transfer effects and 3-dimensional velocity fields.
Methods. We used numerical methods to simultaneously solve the equations of NLTE radiative transfer, statistical equilibrium of hydrogen level populations, and electric neutrality. The radiative transfer equations were solved using cylindrical coordinates and prescribed solar incident radiation. In addition to the effects of anisotropic incident radiation, treated in previous papers, we took into account the Doppler shifts produced by a 3-dimension velocity field.
Results. The effects of different types of velocity fields on hydrogen line profiles and intensities are described. Motions include loop oscillations, rotation, and longitudinal flows, which produce different deformations of profiles. Doppler brightening and dimming effects are also observed.
Conclusions. This is a new step in the diagnostic of physical conditions in coronal loops, allowing the study of dynamical phenomena.

Key words. methods: numerical – radiative transfer – line: formation – line: profiles – Sun: chromosphere – Sun: corona

1. Introduction

The outer solar atmosphere, observed in spectral lines with sufficient opacity or emissivity, appears to be formed of thread-like structures, produced by the magnetic field. Different kinds of motions may be detected within these structures. Instruments with high spatial and spectral resolutions, such as SOHO/SUMER, allow the detection of velocity fields by Doppler effect (see observations by Chae et al. 2000). Imagers with high angular and temporal resolutions directly show the motions of loops (see in particular some movies by TRACE on http://trace.lmsal.com/). The modeling of these structures requires the introduction of the Doppler effect in radiative transfer equations.

This paper is the fifth in a series dedicated to NLTE radiative transfer in cylindrical objects. It is more specifically the continuation of Paper III (Gouttebroze 2006), which dealt with the formation of the hydrogen spectrum in a cylindrical object, taking into account both multilevel-atom and 2-dimensional azimuth-dependent (2DAD) radiative transfer effects. The method for solving 2DAD radiative transfer equations, as well as for determining appropriate boundary conditions, are described in Paper II (Gouttebroze 2005). Other equations, concerning statistical and mechanical equilibrium, are given in Paper I (Gouttebroze 2004).

In the present paper, we introduce a velocity field in the radiative transfer equations for spectral lines. The principal consequence is that the absorption coefficient is now dependent on direction. Some symmetries are lost: line profiles are no longer symmetric with respect to the line center, as it was in the static case. Also, the symmetry in ψ (azimuthal coordinate) is no longer valid, which requires the use of a ψ-mesh covering a range of 2π radians, instead of π in Paper III. The differences in the formulation are explained in Sect. 2, and consequences on the code in Sect. 3. Results are given in Sect. 4 for different types of velocity fields.

2. Formulation

Apart from the presence of velocity fields, the model under consideration is the same as in Paper III, i.e. a cylinder imbedded in the solar corona and filled with a mixture of hydrogen and helium, in the proportion of 1 atom of helium for 10 atoms of hydrogen. Helium is assumed to be neutral, so that the electrons present in the medium come from the ionization of hydrogen. As a consequence, the electron density is equal to the proton density, which is determined by a set of equations including statistical equilibrium of hydrogen level populations, radiative transfer in various transitions, and pressure equilibrium. The temperatures, pressures, and microturbulent velocities inside the cylinder are set a priori, as is the velocity field. Other physical parameters are deduced by solving the above-mentioned system of equations. The introduction of a velocity field leaves a number of equations unchanged, which have been presented in Papers I and II and are not reproduced here. They mainly concern:

- the calculation of incident intensities, taking the specific geometry of the problem into account (Paper II);
- equations of statistical equilibrium, treated in Paper I, which are essentially independent of geometry;
- equations concerning radiative transfer in continua, which are practically insensitive to the Doppler effect, for moderate

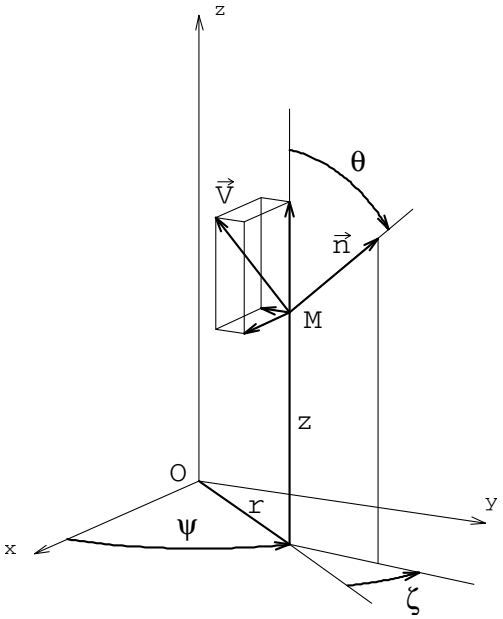

Fig. 1. System of coordidates for the cylinder: the location of the running point is defined by r, ψ and z, the direction of the ray by θ and ζ, and the gas velocity by $\boldsymbol{V}$. The 3 Cartesian components of $\boldsymbol{V}$ are also plotted (without labels).

velocities. The absorption and emission coefficients are given in Paper I, and the 2DAD transfer process is the same as for lines, as described in Paper II.

We thus concentrate here on equations concerning radiative transfer in spectral lines with Doppler effect.

2.1. Systems of coordinates

To solve the present problem, it is convenient to use cylindrical and Cartesian coordinates in parallel. Physical parameters, as well as boundary conditions, are more simply expressed in terms of cylindrical coordinates. In contrast, the direction of a ray crossing the cylinder is defined by constant parameters (direction cosines) in Cartesian coordinates instead of variable angles in a cylindrical system. The coordinate systems are represented in Fig. 1. The running point M is defined by three cylindrical coordinates r, ψ, and z, or alternatively by Cartesian coordinates $x = r\cos\psi$, $y = r\sin\psi$, and z. The direction of a ray at point M is defined either by direction cosines (u, v, w) or by two angles ζ and θ. To cover the whole space, ζ varies from $-\pi$ to π, and θ from 0 to π. However, it will be seen later that, using symmetrized variables, the range of variation in ζ may be reduced to $[-\pi/2, +\pi/2]$. The direction cosines may be deduced from direction angles as

$$\begin{aligned} u &= \sin\theta\cos(\psi+\zeta), \\ v &= \sin\theta\sin(\psi+\zeta), \\ w &= \cos\theta, \end{aligned} \tag{1}$$

and the inverse tranformation may be written

$$\begin{aligned} \zeta &= \begin{cases} \arccos\left(\frac{u}{\sqrt{u^2+v^2}}\right) - \psi, & \text{if } v \geq 0, \\ -\arccos\left(\frac{u}{\sqrt{u^2+v^2}}\right) - \psi, & \text{if } v < 0, \end{cases} \\ \theta &= \arccos w. \end{aligned} \tag{2}$$

The velocity of the gas is defined by the vector $\boldsymbol{V}$, which is a function of r and ψ. The longitudinal component V_z is common to the Cartesian and cylindrical coordinates, while the Cartesian transversal components, V_x and V_y, may be deduced from the cylindrical ones, V_r and V_ψ, by

$$\begin{aligned} V_x &= V_r\cos\psi - V_\psi\sin\psi, \\ V_y &= V_r\sin\psi + V_\psi\cos\psi. \end{aligned} \tag{3}$$

2.2. Absorption coefficient and source function

The absorption coefficient in a spectral line formed between the lower level l and the upper level u may be written

$$\kappa_{lu}(\Delta\nu, \boldsymbol{n}) = \kappa^{\mathrm{M}}_{lu}\phi(\Delta\nu, \boldsymbol{n}), \tag{4}$$

with

$$\kappa^{\mathrm{M}}_{lu} = \frac{h\nu_{ul}}{4\pi}(N_l B_{lu} - N_u B_{ul}). \tag{5}$$

Here, κ^{M}_{lu} is the mean (or frequency-integrated) absorption coefficient, $\Delta\nu$ the frequency difference with the frequency at line center ν_{ul}, N_j the number density of atoms in level j, B_{ij} the Einstein coefficients for absorption or stimulated emission, and ϕ the normalized profile (other symbols have their usual meaning). In the rest frame of the gas, the profile ϕ^{G} is independent of direction, as in the static case, and may be written

$$\phi^{\mathrm{G}}(\Delta\nu^{\mathrm{G}}) = \frac{1}{\sqrt{\pi}\Delta\nu_{\mathrm{D}}} H\left(a, \frac{\Delta\nu^{\mathrm{G}}}{\Delta\nu_{\mathrm{D}}}\right) \tag{6}$$

where H is the Voigt function, $\Delta\nu^{\mathrm{G}}$ the relative frequency in the rest frame of the gas, $\Delta\nu_{\mathrm{D}}$ the Doppler width, and a the damping factor.

As a result of the Doppler effect, a photon with a relative frequency $\Delta\nu^{\mathrm{G}}$ in the rest frame of the gas, with a direction $\boldsymbol{n}$, is observed in a fixed frame with a relative frequency $\Delta\nu$ such that

$$\Delta\nu^{\mathrm{G}} = \Delta\nu - \frac{\nu_{ul}}{c}\boldsymbol{n}\cdot\boldsymbol{V}, \tag{7}$$

which yields the profile in the fixed frame

$$\phi(\Delta\nu, \boldsymbol{n}) = \frac{1}{\sqrt{\pi}\Delta\nu_{\mathrm{D}}} H\left[a, \frac{1}{\Delta\nu_{\mathrm{D}}}\left(\Delta\nu - \frac{\nu_{ul}}{c}\boldsymbol{n}\cdot\boldsymbol{V}\right)\right]. \tag{8}$$

Since the Voigt function is symmetric, from Eq. (8) the useful relation follows

$$\phi(-\Delta\nu, -\boldsymbol{n}) = \phi(\Delta\nu, \boldsymbol{n}). \tag{9}$$

Under the assumptions of complete redistribution and negligible continuous absorption, ϕ is also the emission profile, so that the source function is, as in the static case, independent of frequency and direction, i.e.,

$$S_{lu} = \frac{N_u A_{ul}}{N_l B_{lu} - N_u B_{ul}}. \tag{10}$$

2.3. Radiative transfer along a ray

The equation of transfer may be written

$$\frac{\mathrm{d}I(\Delta\nu, \boldsymbol{n})}{\mathrm{d}s} = \kappa(\Delta\nu, \boldsymbol{n})\,[S_{lu} - I(\Delta\nu, \boldsymbol{n})] \tag{11}$$

where I is the specific intensity and s the abscissa along the ray. We replace the intensity by Feautrier-type variables Y and Z,

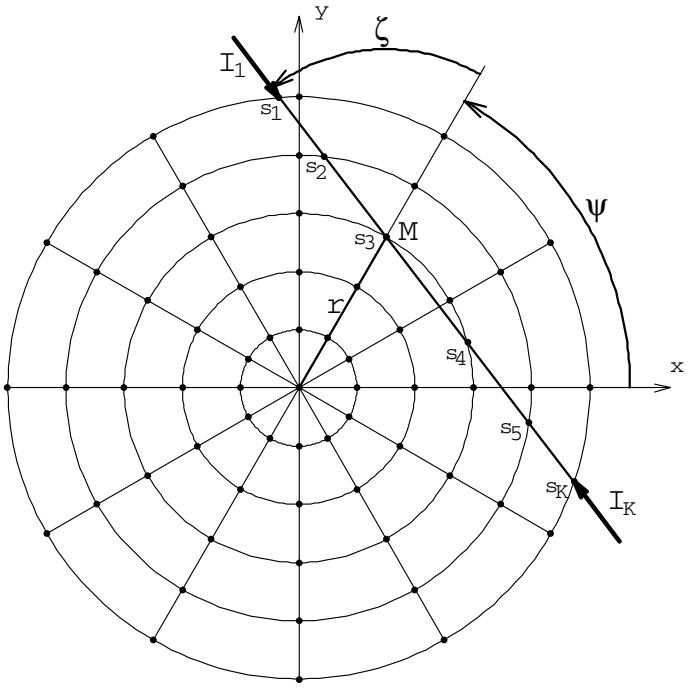

Fig. 2. Path of a photon through the cylinder, projected on a transversal plane (for clarity, the r-mesh is reduced to 6 points).

but associating negative $\boldsymbol{n}$ with negative $\Delta\nu$ to take advantage of Eq. (9), i.e.,

$$\begin{aligned} Y(\Delta\nu,\boldsymbol{n}) &= \frac{1}{2}\left[I(\Delta\nu,\boldsymbol{n}) + I(-\Delta\nu,-\boldsymbol{n})\right], \\ Z(\Delta\nu,\boldsymbol{n}) &= \frac{1}{2}\left[I(\Delta\nu,\boldsymbol{n}) - I(-\Delta\nu,-\boldsymbol{n})\right]. \end{aligned} \tag{12}$$

Applying Eq. (11) to the intensities going in opposite directions and combining the results, we obtain

$$\begin{aligned} \frac{\mathrm{d}Z(\Delta\nu,\boldsymbol{n})}{\mathrm{d}s} &= \kappa(\Delta\nu,\boldsymbol{n})\left[S_{lu} - Y(\Delta\nu,\boldsymbol{n})\right], \\ \frac{\mathrm{d}Y(\Delta\nu,\boldsymbol{n})}{\mathrm{d}s} &= -\kappa(\Delta\nu,\boldsymbol{n})Z(\Delta\nu,\boldsymbol{n}), \end{aligned} \tag{13}$$

and subsequently a second-degree equation for Y,

$$-\frac{1}{\kappa(\Delta\nu,\boldsymbol{n})}\frac{\mathrm{d}}{\mathrm{d}s}\left[\frac{1}{\kappa(\Delta\nu,\boldsymbol{n})}\frac{\mathrm{d}Y(\Delta\nu,\boldsymbol{n})}{\mathrm{d}s}\right] + Y(\Delta\nu,\boldsymbol{n}) = S_{lu}. \tag{14}$$

This equation has a familiar form and may be, by discretization of s, transformed into a tridiagonal system to deduce Y from S. To close the system, we use the boundary conditions provided by the incident intensities at both ends of the ray, I_1 and I_K (corresponding to the extreme values of s, named s_1 and s_K),

$$\begin{aligned} \left[Y(\Delta\nu,\boldsymbol{n}) - \frac{1}{\kappa(\Delta\nu,\boldsymbol{n})}\frac{\mathrm{d}Y(\Delta\nu,\boldsymbol{n})}{\mathrm{d}s}\right]_{s_1} &= I_1(\Delta\nu,\boldsymbol{n}), \\ \left[Y(\Delta\nu,\boldsymbol{n}) + \frac{1}{\kappa(\Delta\nu,\boldsymbol{n})}\frac{\mathrm{d}Y(\Delta\nu,\boldsymbol{n})}{\mathrm{d}s}\right]_{s_K} &= I_K(-\Delta\nu,-\boldsymbol{n}). \end{aligned} \tag{15}$$

It should be noticed that, since the incident intensities are expressed in a fixed frame, they are symmetric with respect to $\Delta\nu$. As a consequence, it is sufficient to compute one half-profile for each line, as in Papers II and III.

2.4. Mean intensity

The mean intensity, which is used in the equations of statistical equilibrium of level populations, is obtained by integrating the specific intensity, multiplied by the absorption profile, with respect to frequency and direction, i.e.,

$$\bar{J} = \frac{1}{4\pi}\int_{-\infty}^{+\infty}\mathrm{d}(\Delta\nu)\oint I(\Delta\nu,\boldsymbol{n})\phi(\Delta\nu,\boldsymbol{n})\mathrm{d}\Omega. \tag{16}$$

The integration over the whole Ω-space may be split into two half spaces, which gives, in terms of direction angles,

$$\oint f(\boldsymbol{n})\mathrm{d}\Omega = \int_{-\pi/2}^{+\pi/2}\mathrm{d}\zeta\int_0^{\pi}\left[f(\boldsymbol{n}) + f(-\boldsymbol{n})\right]\sin\theta\,\mathrm{d}\theta. \tag{17}$$

Applying this formula to Eq. (16) and distinguishing between positive and negative relative frequencies, we obtain

$$\begin{aligned} \bar{J} &= \frac{1}{4\pi}\int_0^{\infty}\mathrm{d}(\Delta\nu)\int_{-\pi/2}^{+\pi/2}\mathrm{d}\zeta\int_0^{\pi}\left[I(\Delta\nu,\boldsymbol{n})\phi(\Delta\nu,\boldsymbol{n})\right. \\ &+ I(\Delta\nu,-\boldsymbol{n})\phi(\Delta\nu,-\boldsymbol{n}) + I(-\Delta\nu,\boldsymbol{n})\phi(-\Delta\nu,\boldsymbol{n}) \\ &+ \left. I(-\Delta\nu,-\boldsymbol{n})\phi(-\Delta\nu,-\boldsymbol{n})\right]\sin\theta\,\mathrm{d}\theta. \end{aligned} \tag{18}$$

Using Eqs. (9) and (12), this expression reduces to

$$\begin{aligned} \bar{J} &= \frac{1}{2\pi}\int_{-\pi/2}^{+\pi/2}\mathrm{d}\zeta\int_0^{\pi}\sin\theta\,\mathrm{d}\theta\int_{-\infty}^{+\infty}Y(\Delta\nu,\boldsymbol{n}) \\ &\times \phi(\Delta\nu,\boldsymbol{n})\mathrm{d}(\Delta\nu). \end{aligned} \tag{19}$$

In the case where the intensity would be uniformly equal to unity, $\bar{J}$ should also be equal to 1, which gives the normalization condition for the absorption profile,

$$\frac{1}{2\pi}\int_{-\pi/2}^{+\pi/2}\mathrm{d}\zeta\int_0^{\pi}\sin\theta\,\mathrm{d}\theta\int_{-\infty}^{+\infty}\phi(\Delta\nu,\boldsymbol{n})\mathrm{d}(\Delta\nu) = 1. \tag{20}$$

3. Numerical methods

The formal solution consists of computing the mean intensity $\bar{J}$ at every point inside the cylinder, knowing the absorption coefficients and source functions at these points and the incident intensities at the surface of the cylinder. In the computation of the mean intensity, we successively consider the $(N_r - 1) \times N_\psi$ points of the spatial grid (r_1, which corresponds to the axis of the cylinder, is omitted). From every point M of the spatial mesh, we draw $N_\zeta \times N_\theta$ rays and solve the transfer equation along each of these rays to obtain the symmetrized intensities Y. This operation is repeated for each frequency in the line. Then, we integrate over frequency and direction to obtain $\bar{J}$ at point M, according to Eq. (19).

3.1. Computation of Y

The process is similar to the one described in Paper II. However, there are two important differences:

- there is no more symmetry with respect to the meridian plane containing the center of the Sun. Thus, we use a ψ-mesh covering a range $[0, 2\pi]$ instead of $[0, \pi]$;
- the absorption coefficient depends on direction, i.e. on angles ζ and θ, in addition to other variables like r, ψ, $\Delta\nu$, and transition number, so the full storage of absorption coefficients could be problematic. It was found to be more convenient

to store the mean absorption coefficient of the line $\kappa^{\rm M}$ (independent of ζ, θ, and $\Delta\nu$) and the parameters $\Delta\nu_{\rm D}$ and a, mentioned in Eq. (6), separately. At each position on the ray, the absorption profile may be recomputed from these two parameters and from the velocity vector $\boldsymbol{V}$.

The path of a photon through the cylinder is represented in Fig. 2 in projection on a transversal plane. The angle θ is not represented, so that one ray on the figure corresponds to N_θ rays in three dimensions. The different variables are discretized: there are N_r values r_i for the radius, N_ψ for the azimuth, and N_ζ and N_θ for the direction angles. For the relative frequency $\Delta\nu$, we keep a mesh covering one half-profile ($\Delta\nu_\gamma, \gamma = 1, \ldots, n$), as in the previous codes, and apply it twice to cover the whole profile.

The incident intensities at both ends, I_1 and I_K, and the level populations for each point of the spatial mesh, are known. From the level populations, the source functions and the frequency-integrated absorption coefficients may be computed for each point of the spatial mesh (r and ψ). Parameters $\Delta\nu_{\rm D}$ and a are determined from the local temperature and microturbulent velocity. Using the trigonometric interpolation procedure described in the next section, we may obtain the values of these parameters for any ψ. The transfer Eq. (14) is discretized along a mesh formed by the intersections of the ray with the cylinders corresponding to the radius mesh (represented by circles in Fig. 2). The number of the intersections K is variable with r and ζ, its maximum value being $(2N_r - 2)$. For each of these intersections ($j = 1, \ldots, K$), the abscissa s_j is determined, as well as the absorption coefficient κ_j and the source function S_j. The discretization of Eq. (14) produces a tridiagonal system

$$-A_j Y_{j-1} + \left(1 + A_j + C_j\right) Y_j - C_j Y_{j+1} = S_j, \quad (j = 2, \ldots, K-1), \tag{21}$$

with

$$A_j = \frac{4}{\kappa_j (s_{j+1} - s_{j-1})(\kappa_{j-1} + \kappa_j)(s_j - s_{j-1})}, \tag{22}$$

and

$$C_j = \frac{4}{\kappa_j (s_{j+1} - s_{j-1})(\kappa_j + \kappa_{j+1})(s_{j+1} - s_j)}. \tag{23}$$

This system is complemented by the boundary conditions (15), whose dicretized form is

$$\begin{aligned} (1 + C_1 + H_1)\, Y_1 - C_1 Y_2 &= S_1 + H_1 I_1, \\ -A_K Y_{K-1} + (1 + A_K + H_K)\, Y_K &= S_K + H_K I_K, \end{aligned} \tag{24}$$

with $C_1 = 2/[\kappa_1^2 (s_2 - s_1)^2]$, $H_1 = 2/[\kappa_1 (s_2 - s_1)]$, $A_K = 2/[\kappa_K^2 (s_K - s_{K-1})^2]$, and $H_K = 2/[\kappa_K (s_K - s_{K-1})]$. (For the derivation of these formulae, see Paper II.) This system is solved in the usual manner to obtain the values of Y along the ray, and the value at point M is retained.

3.2. Trigonometric interpolation

The numerical solution of the radiative transfer equation using the intersections of the ray with the radius mesh cylinders as mesh points, there is no need for interpolation in r. In contrast, to determine the coefficients of Eqs. (21) to (24), it is necessary to interpolate in ψ several parameters, namely, $\kappa^{\rm M}$, S, $\Delta\nu_{\rm D}$, and a. The velocity vector $\boldsymbol{V}$ is not interpolated, but defined as a function of r and ψ.

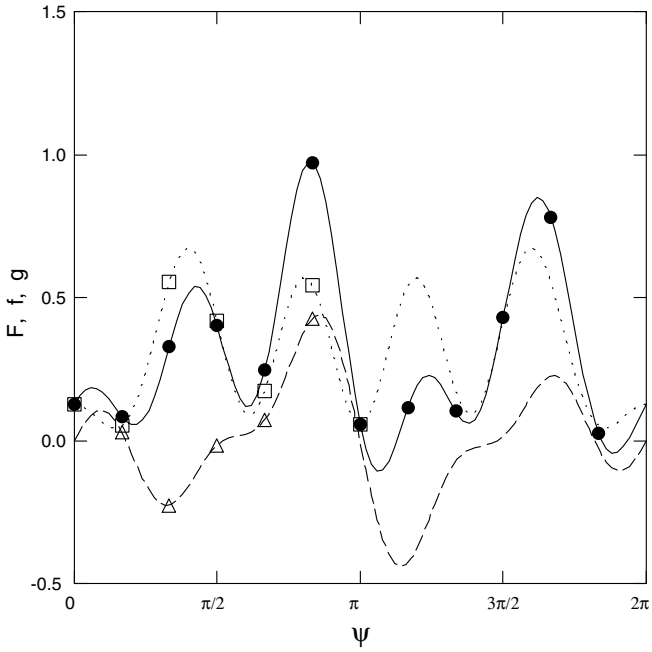

Fig. 3. Example of trigonometric interpolation. For a regularly spaced ψ-mesh, $2m$ values F_j are randomly chosen (here, $m = 6$). They are represented by full circles. The $(m + 1)$ values f_j (open squares) and $(m - 1)$ values g_j (open triangles) are deduced according to Eqs. (31) and (32). The points f_j are fit by the even function $f(\psi)$ (dotted line) and g_j by the odd function $g(\psi)$ (dashed line). The sum of these two functions $F(\psi)$ (full line) fits the original data.

As said above, there is no longer any symmetry in ψ, so that we use a ψ-mesh covering the interval $[0, 2\pi]$, viz.

$$\psi_j = \frac{2\pi(j-1)}{N_\psi}, \quad (j = 1, \ldots, N_\psi), \tag{25}$$

where N_ψ is even ($N_\psi = 2m$). The function to be interpolated is defined on the same grid, i.e.,

$$F(\psi_j) = F_j, \quad (j = 1, \ldots, N_\psi). \tag{26}$$

The interpolation procedure consists of splitting the function into its even and odd parts, respectively,

$$\begin{aligned} f(\psi) &= \frac{1}{2}\left[F(\psi) + F(2\pi - \psi)\right] \quad \text{and} \\ g(\psi) &= \frac{1}{2}\left[F(\psi) - F(2\pi - \psi)\right], \end{aligned} \tag{27}$$

and replacing $f(\psi)$ by a series of cosines and $g(\psi)$ by a series of sines. Since the sine functions vanish for $\psi = 0$ and $\psi = \pi$, the two series have an unequal number of terms, $(m + 1)$ for $f(\psi)$ and $(m - 1)$ for $g(\psi)$, i.e.,

$$\begin{aligned} f(\psi) &= \sum_{j=1}^{m+1} a_j \cos[(j-1)\psi] \quad \text{and} \\ g(\psi) &= \sum_{j=2}^{m} b_j \sin[(j-1)\psi]. \end{aligned} \tag{28}$$

The coefficients a_j and b_j are determined by solving a set of $2m$ linear equations, which may be written

$$\sum_{k=1}^{m+1} A_{jk} a_k = f_j, \quad (j = 1, \ldots, m+1), \quad \text{and}$$

$$\sum_{k=2}^{m} B_{jk} b_k = g_j, \quad (j = 2, \ldots, m), \tag{29}$$

with

$$A_{jk} = \cos[(k-1)\psi_j] = \cos\frac{\pi(k-1)(j-1)}{m}, \quad \text{and}$$
$$B_{jk} = \sin\frac{\pi(k-1)(j-1)}{m}. \tag{30}$$

It should be noticed that, as a result of the orthogonality properties of trigonometric functions, the matrices A and B may be inverted by analytical means (cf. Legras 1963). The coefficients f_j and g_j are obtained from the F_j as

$$\begin{aligned} f_1 &= F_1, \\ f_j &= \frac{1}{2}(F_j + F_{2m+2-j}), \quad (j = 2, \ldots, m), \\ f_{m+1} &= F_{m+1}, \end{aligned} \tag{31}$$

and

$$g_j = \frac{1}{2}(F_j - F_{2m+2-j}), \quad (j = 2, \ldots, m). \tag{32}$$

An example of this method of interpolation is shown in Fig. 3.

3.3. Integration over frequency and direction

The quadrature formulae for direction are the same as in the static case. For ζ, we have

$$\frac{1}{\pi}\int_{-\pi/2}^{+\pi/2} f(\zeta)\mathrm{d}\zeta \approx \sum_{\alpha=1}^{l} a_\alpha f(\zeta_\alpha), \tag{33}$$

and, for θ,

$$\frac{1}{2}\int_0^{\pi} f(\theta)\sin\theta\mathrm{d}\theta \approx \sum_{\beta=1}^{m} b_\beta f(\theta_\beta). \tag{34}$$

The situation for frequency is different, since we must integrate over the whole profile, which is assymmetric. Considering one half profile, we limit it to its useful part $[0, \Delta\nu_{\max}]$ and introduce a quadrature formula,

$$\int_0^{\Delta\nu_{\max}} f(\Delta\nu)\mathrm{d}(\Delta\nu) \approx \sum_{\gamma=1}^{n} c_\gamma f(\Delta\nu_\gamma). \tag{35}$$

Substituting the three preceding formulae into Eq. (19), we obtain

$$\begin{aligned} \bar{J} = &\sum_{\alpha=1}^{l} a_\alpha \sum_{\beta=1}^{m} b_\beta \sum_{\gamma=1}^{n} c_\gamma [Y(\Delta\nu_\gamma, \zeta_\alpha, \theta_\beta)\phi(\Delta\nu_\gamma, \zeta_\alpha, \theta_\beta) \\ &+ Y(-\Delta\nu_\gamma, \zeta_\alpha, \theta_\beta)\phi(-\Delta\nu_\gamma, \zeta_\alpha, \theta_\beta)]. \end{aligned} \tag{36}$$

The normalization condition (20) gives

$$\sum_{\alpha=1}^{l} a_\alpha \sum_{\beta=1}^{m} b_\beta \sum_{\gamma=1}^{n} c_\gamma [\phi(\Delta\nu_\gamma, \zeta_\alpha, \theta_\beta) + \phi(-\Delta\nu_\gamma, \zeta_\alpha, \theta_\beta)] = 1. \tag{37}$$

In practice, to ensure a good normalization of the integration process (conservation of photons), we compute the lefthand side of Eq. (37) and divide the result of Eq. (36) by this value.

3.4. Preconditioning

To accelerate the Λ-iteration according to the "MALI" method, we use as approximate operator the diagonal of the full Λ operator, as suggested by Olson et al. (1986). The tridiagonal system formed by Eqs. (21) and (24) may be formally written as a matrix product

$$M\boldsymbol{Y} = \boldsymbol{S} + \boldsymbol{I}^{\mathbf{inc}}, \tag{38}$$

where $\boldsymbol{I}^{\mathbf{inc}} = [H_1 I_1, 0, \ldots, 0, H_K I_K]$. If W is the inverse of the tridiagonal matrix M, the solution of Eq. (38) is obviously

$$\boldsymbol{Y} = W\boldsymbol{S} + W\boldsymbol{I}^{\mathbf{inc}}. \tag{39}$$

We apply the summation operator of Eq. (36), noted for convenience as $\sum_{\alpha\beta\gamma}$, to the two sides of Eq.(39), and obtain

$$\bar{\boldsymbol{J}} = \Lambda\boldsymbol{S} + \boldsymbol{C}, \tag{40}$$

with $\bar{\boldsymbol{J}} = \sum_{\alpha\beta\gamma}(\boldsymbol{Y})$, $\Lambda = \sum_{\alpha\beta\gamma}(W)$, and $\boldsymbol{C} = \sum_{\alpha\beta\gamma}(W\boldsymbol{I}^{\mathbf{inc}})$. When solving the tridiagonal system formed by Eqs. (21) and (24), we obtain the diagonal W^* of the matrix W, according to the method of Rybicki & Hummer (1991, Appendix B), for each ray, and, by summation, the diagonal Λ^* of the Λ operator,

$$\Lambda^* = \sum_{\alpha\beta\gamma}(W^*). \tag{41}$$

The implementation of Λ^* into the equations of statistical equilibrium, according to the principles of Werner & Husfeld (1985), is described in Paper I.

4. Results

Different phenomena may produce motions of matter inside flux tubes. There is an abundant literature concerning the oscillations of coronal loops (see for instance Roberts 2002, and references therein). They primarily produce transversal motions. But there are phenomena, like siphon flows, that produce longitudinal motions (e.g. Robb & Cally 1992; Betta et al. 1999, or Doyle et al. 2006). The purpose of the present paper is not to propose a detailed modeling of these solar phenomena, but rather to study the effects of some basic types of motions (radial, rotational, or longitudinal) on the emitted hydrogen lines.

4.1. Basic static model

The different numerical experiments presented here are based on the same static model, to which we add different velocity fields. This basic model is taken from Paper III, where it was used to study loops with a radial temperature gradient. It consists of a semi-toric loop, whose axis is a circle of radius 10^4 km. The section of the torus is a circle of radius 10^3 km. The axis of the torus is vertical at the feet of the loop and horizontal at the top. The gas pressure is kept constant throughout the loop and equal to 0.1 dyn cm^{-2}. The temperature is only a function of r, equal to 6000 K from $r = 0$ to $r = 500$ km, and regularly growing from $r = 500$ to $r = 1000$ km, where it reaches 10^5 K. This variation is explained in Table 1. Since the numerical code deals with cylinders, the torus is simulated by a succession of tangent cylinders. Each part is characterized by an inclination angle α, going from 0 at the foot of the loop to $\pi/2$ at the top. For each value of the α-grid, a cylindrical model is computed. An interpolation procedure is used to obtain physical and spectroscopic parameters

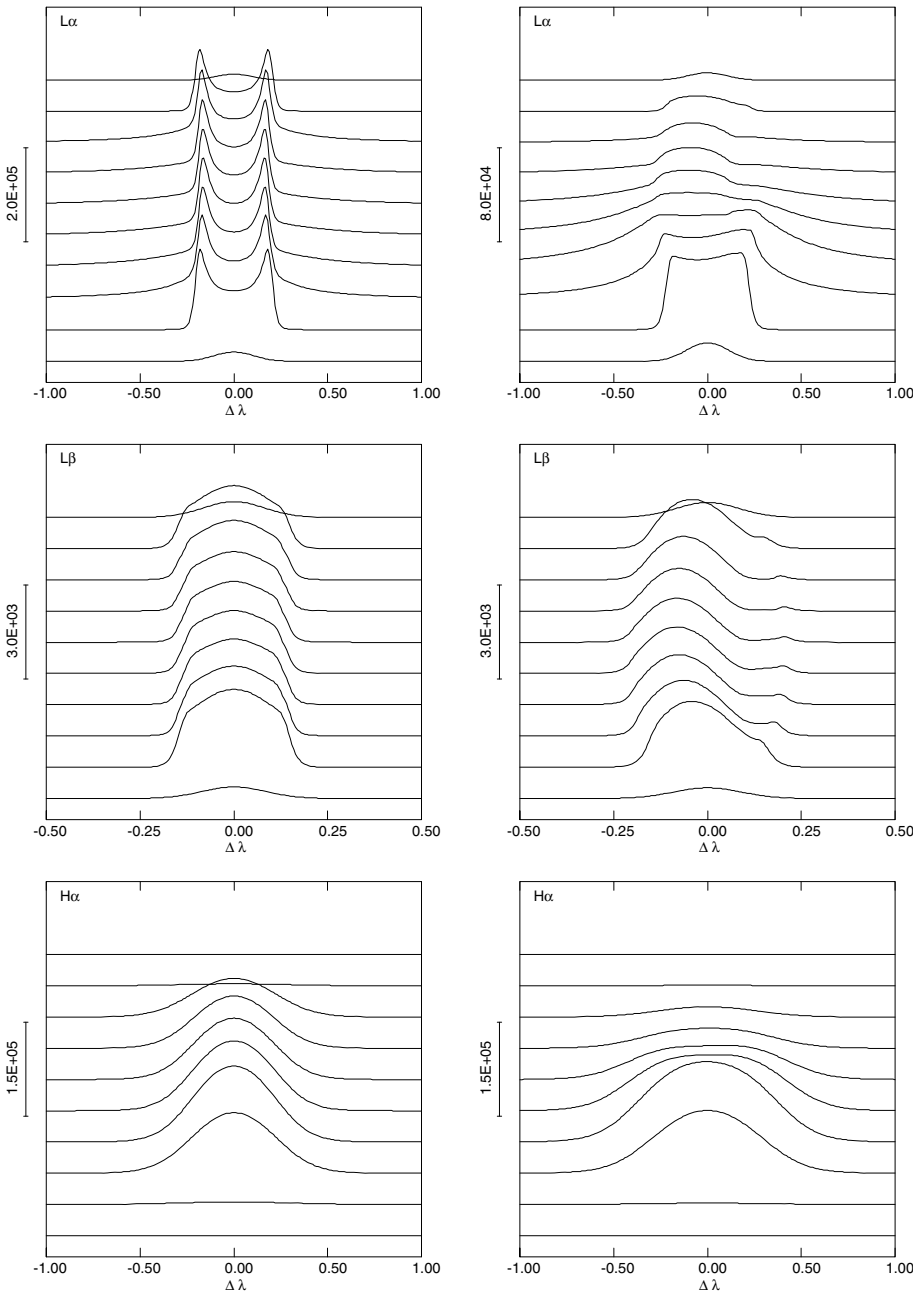

Fig. 4. Intensity variations across the *top* of the loop for 10 equidistant positions (every 200 km). At *left*: line profiles for the static model. At *right*: profiles for a radial velocity of 30 km s^{-1} at the boundary. *Top*: Lα line; *middle*: Lβ; *bottom*: Hα. Abscissae are relative wavelengths in Å. For clarity, each curve is shifted upwards with respect to the preceding one. The intensity scale for each panel is indicated at *left*, in erg cm^{-2} s^{-1} sr^{-1} $Å^{-1}$.

Table 1. Physical parameters and optical thicknesses at selected points of the *r*-grid, in the static model (at the foot of the loop: vertical axis).

r (km)	T (K)	N_H (cm^{-3})	$\frac{N_e}{N_H}$	τ(Lα)	τ(Lβ)	τ(Hα)
0.00	6000.	9.17E+10	0.216	2.51E+05	4.03E+04	4.09E–01
93.10	6000.	9.16E+10	0.218	2.06E+05	3.30E+04	3.57E–01
186.21	6000.	9.11E+10	0.225	1.61E+05	2.58E+04	3.04E–01
279.31	6000.	9.02E+10	0.238	1.17E+05	1.88E+04	2.47E–01
372.41	6000.	8.88E+10	0.260	7.47E+04	1.20E+04	1.85E–01
465.52	6000.	8.61E+10	0.302	3.49E+04	5.59E+03	1.14E–01
527.59	7008.	6.82E+10	0.414	1.26E+04	2.03E+03	6.20E–02
620.69	11 833.	3.24E+10	0.791	1.23E+03	1.97E+02	1.60E-02
713.79	19 980.	1.75E+10	0.976	4.30E+01	6.90E+00	5.51E-04
806.90	33 738.	1.02E+10	0.999	9.07E–01	1.45E–01	4.33E–06
900.00	56 968.	6.05E+09	1.000	4.83E–02	7.75E–03	1.91E–07
990.00	94 529.	3.65E+09	1.000	1.18E–03	1.89E–04	4.46E–09
999.00	99 439.	3.47E+09	1.000	1.06E–04	1.70E–05	4.02E–10
999.90	99 944.	3.45E+09	1.000	1.05E–05	1.68E–06	3.98E–11
1000.0	100 000.	3.45E+09	1.000	0.0	0.0	0.0

Table 2. Optical thicknesses for the static model, at the top of the loop (horizontal axis).

Transition	Line	$\psi = 0$	$\psi = \pi/2$	$\psi = \pi$
1–2	Lα	2.54E+05	2.71E+05	2.91E+05
1–3	Lβ	4.07E+04	4.35E+04	4.67E+04
2–3	Hα	4.66E–01	4.03E–01	3.33E–01
1–4	Lγ	1.41E+04	1.51E+04	1.62E+04
2–4	Hβ	6.45E–02	5.57E–02	4.60E–02
3–4	Pα	7.07E–03	5.46E–03	4.05E–03
1–5	Lδ	6.64E+03	7.09E+03	7.62E+03
2–5	Hγ	2.15E–02	1.86E–02	1.54E–02
3–5	Pβ	9.42E–04	7.31E–04	5.45E–04
4–5	Brα	2.99E–03	2.45E–03	1.92E–03

corresponding to intermediate values of α. Once the temperature, pressure, and microturbulent velocity (fixed to 5 km s^{-1}) are set, the other parameters are computed by solving the equations of radiative transfer, statistical equilibrium, pressure equilibrium, and electric neutrality (the incident intensities in different lines and continua of hydrogen are also set, as described in previous papers). The physical parameters resulting from this computation, such as hydrogen and electron densities, are functions of both r and ψ. An exception is the foot of the loop: there, the incident radiation is independent of ψ, so that the transfer problem reduces to one dimension, and all physical parameters only depend on r. In Table 1, the total hydrogen density $N_{\rm H}$ and the ionization ratio ($N_{\rm e}/N_{\rm H}$) are given as functions of r, for the foot of the loop. In addition, this table gives optical thicknesses, between the running point and the surface, for three basic transitions of hydrogen (Lα, Lβ, and Hα). The comparison of optical thicknesses of Lyman and Balmer lines explains why the same loop appears to be broader in UV than in visible observations. The total optical thicknesses (between the axis and the surface of the cylinder) are displayed in Table 2 for a larger set of transitions. Here, the values correspond to the top of the loop, where the axis is horizontal. In this case, the incident intensities and the resulting physical parameters depend on azimuth, so we give the thicknesses for three values of ψ: 0 (vertical downward direction), $\pi/2$ (horizontal), and π (vertical upward). Since the incident intensities from the Sun decrease as ψ increases, the excitation of hydrogen atoms decreases. The result is an increase in optical thicknesses in Lyman lines, in proportion to the population of the ground state, and conversely a decrease in thicknesses in other lines, whose lower levels are less and less excited.

4.2. Radial motions

We consider a radial velocity V_r, which could correspond to a phase of expansion during a process of radial oscillation. The radial velocity is taken as proportional to the distance to the axis, i.e. $V_r = k\ r$. Three values of k have been tested: 0.01, 0.02, and 0.03 s^{-1}. The highest value, which corresponds to a radial velocity of 30 km s^{-1} at the surface of the cylinder, produces line profiles that are displayed in Fig. 4. Each individual profile corresponds to one different position across the top of the loop (equivalent to a cylinder with horizontal axis). The deformation of profiles is particularly important for Lyman-α, as may be seen at the top of Fig. 4. In addition, the comparison of intensity scales for static and expanding models shows that Lα is strongly affected by the Doppler dimming effect (studied for planar models by Heinzel & Rompolt 1987; Gontikakis et al. 1997a,b; or Labrosse et al. 2007). The Lα profiles corresponding to intermediate radial velocities (10 and 20 km s^{-1} at boundary)

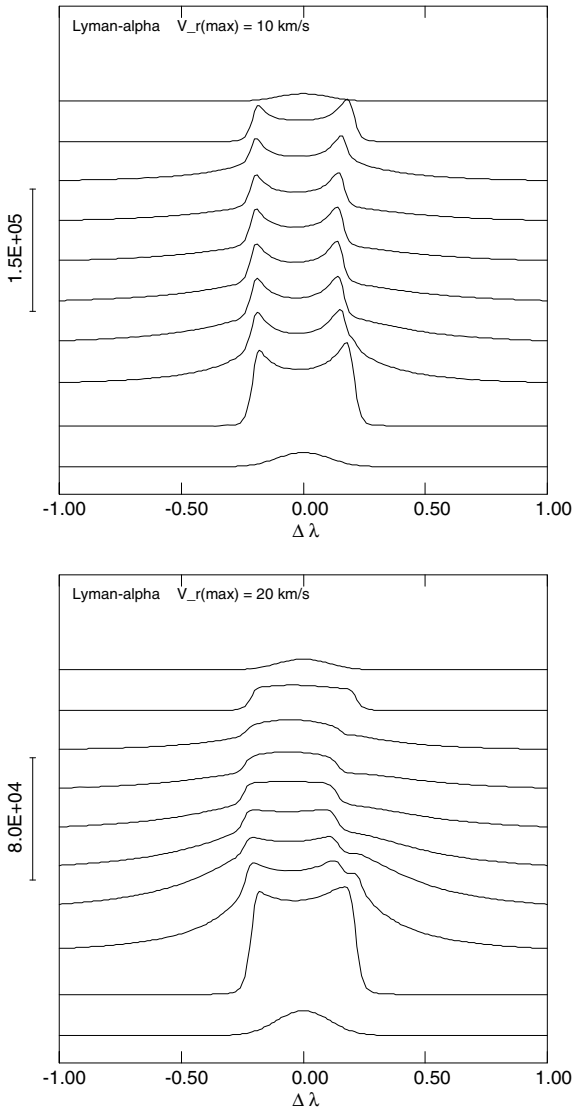

Fig. 5. Intensity variations across the *top* of the loop for the Lα line, for intermediate radial velocities. *Top*: 10 km s^{-1} at boundary; *bottom*: 20 km s^{-1}. Same units and positions as in Fig. 4.

are displayed in Fig. 5 to show the gradual transformation of the profiles. Intensities in the other hydrogen lines are much less affected by the radial velocity. For Lβ, there are two maxima in the profiles. The main peak, shifted towards the blue, corresponds to the front part of the cylinder. A much weaker peak, appearing in the red side of the line, is produced by the rear part of the structure. This effect is shown in Fig. 6 as a gray image with higher spatial resolution (201 points, i.e. 10 km). Upper Lyman lines (not represented here) exhibit the same behavior as the Lβ line. Balmer lines (represented here by Hα) are esentially broadened by the radial velocity. When the velocity field is present, their intensity in the upper part of the cylinder is somewhat lowered with respect to the static case. This effect may be due to the broadening of the absorption profile in the lower part of the cylinder, which tends to reduce the penetration of incident radiation in the upper part.

4.3. Rotation

In this case, we apply a rotational motion of the cylinder around its axis. This rotation is of the solid type, i.e. $V_\psi = \omega_0 r$. The

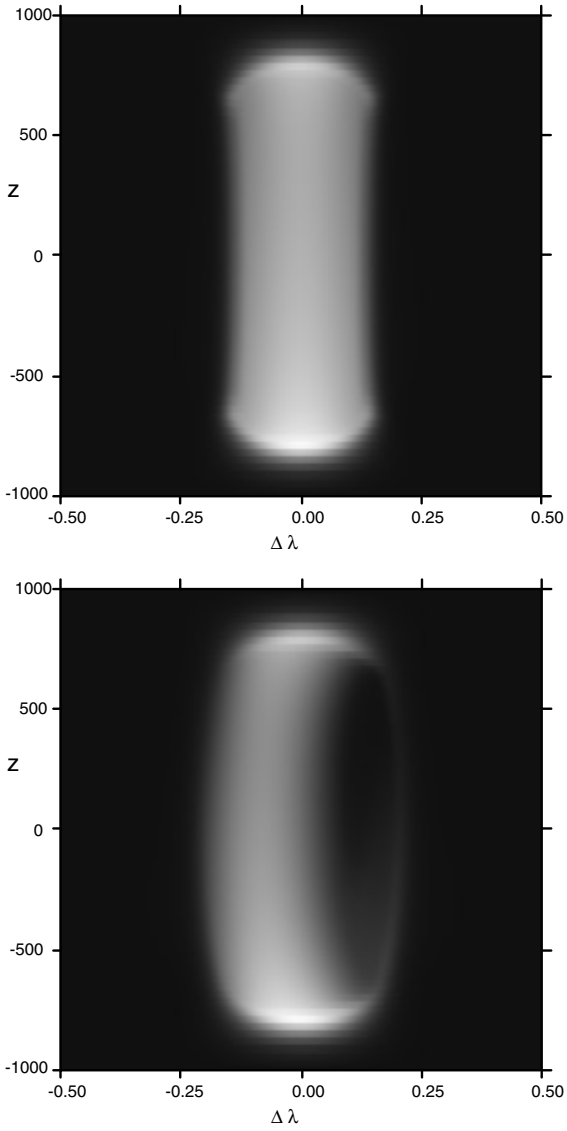

Fig. 6. Intensity variations across the top of the loop for the Lβ line (relative scale; white corresponds to brightest points). Abscissae: relative wavelengths (Å). Ordinates: distances in km. *Top*: static case; *bottom*: expanding model (30 km s^{-1} at boundary).

angular velocity ω_0 used here is equal to 0.02 rad s^{-1}, so that the tangential velocity is 20 km s^{-1} at boundary. Contrary to the radial velocities, the tangential ones have little influence on the intensities and the shape of the profiles. The main effect, for a horizontal cylinder, is a shift of the profiles, to the red in the upper part of the structure and to the blue in the lower part, according to the Doppler effect. These profiles are displayed in Fig. 7 for Lα, Lβ, and Hα, to compare with the static profiles of Fig. 4. For Lβ, a representation as image is provided in Fig. 8, for comparison with Fig. 6.

4.4. Longitudinal flow

The effects of longitudinal flows are studied using two values of the velocity V_z, 30 and 80 km s^{-1}. It appears that this kind of motion has little influence on the Lα profile and intensity, except a slight dimming effect. A stronger effect may be observed on Lβ: the profiles are significantly broadened and take a square shape (Fig. 9), at least for the highest velocity. There

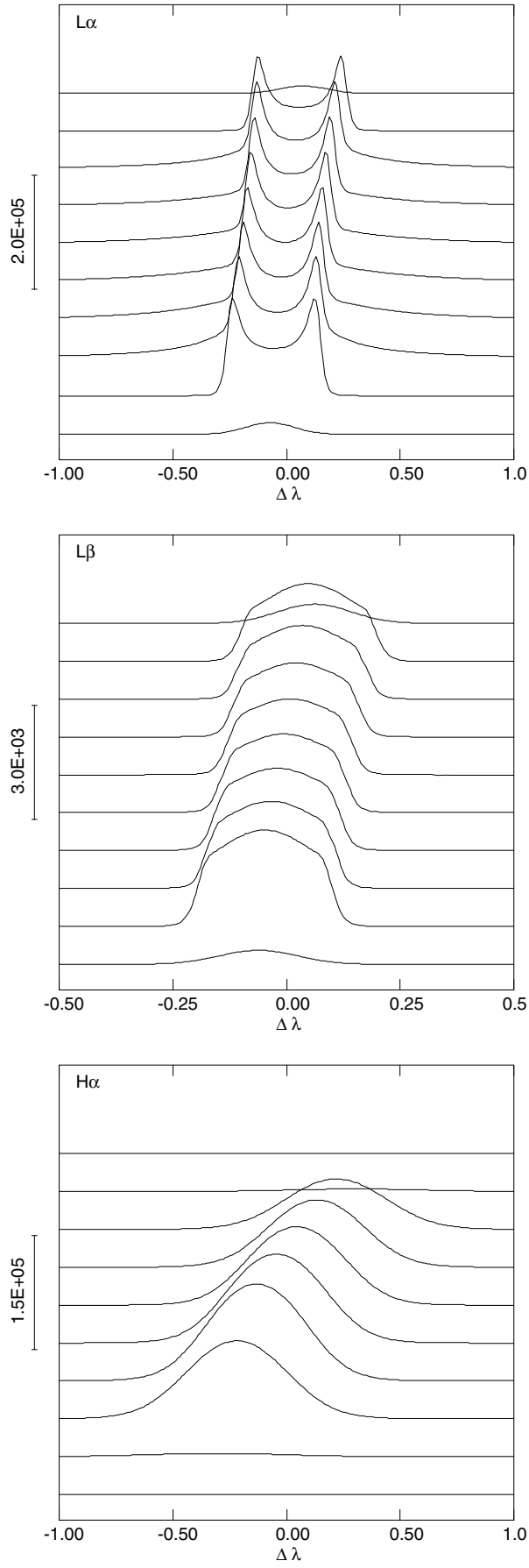

Fig. 7. Same as the right part of Fig. 4, but for a rotational motion with angular velocity ω_0 = 0.02 rad s^{-1}.

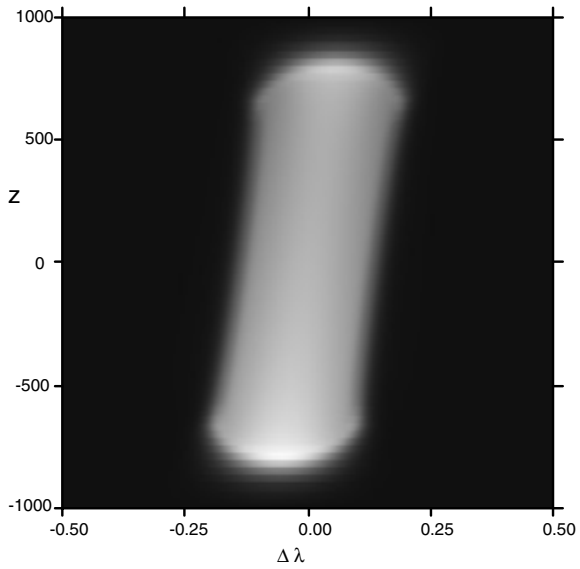

Fig. 8. Same as Fig. 6 (Lβ), for a rotational motion with angular velocity $\omega_0 = 0.02$ rad s^{-1}.

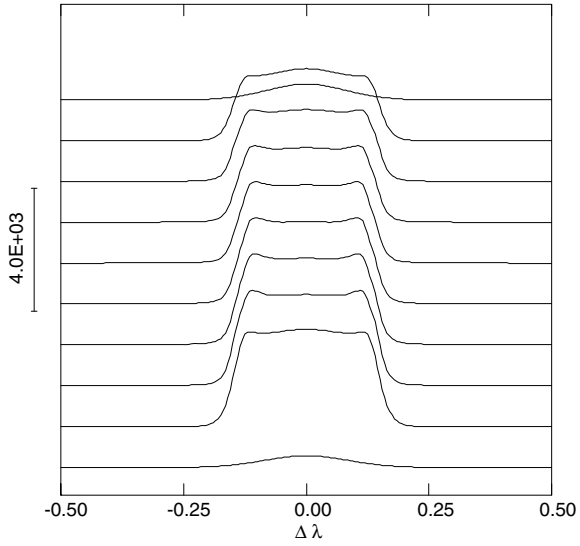

Fig. 9. Intensity profiles of Lβ, for a longitudinal velocity V_z = 80 km s^{-1} (same presentation and units as in Fig. 4).

is also an increase in intensity. For Hα, the shape of the profiles remains nearly Gaussian, but the intensity increases rapidly. This Doppler-brightening effect for Hα and Lβ is illustrated by Fig. 10. The ratio of intensities, along the axis of the loop, between the dynamic and the static models, is plotted as a function of the inclination angle α. The highest ratio is observed for Hα, whatever the inclination angle. For Hα as for Lβ, these effects are somewhat stronger near the feet of the loop ($\alpha = 0$) than near the top ($\alpha = \pi/2$).

5. Conclusion

The numerical methods developed here constitute a new step in modeling the filamentary structures observed in the solar chromosphere and corona. The code described in Paper III was able to treat NLTE radiative transfer for a multilevel hydrogen atom in a 2D azimuth-dependent cylindrical geometry. To these functionalities, the present code adds the possibility of treating

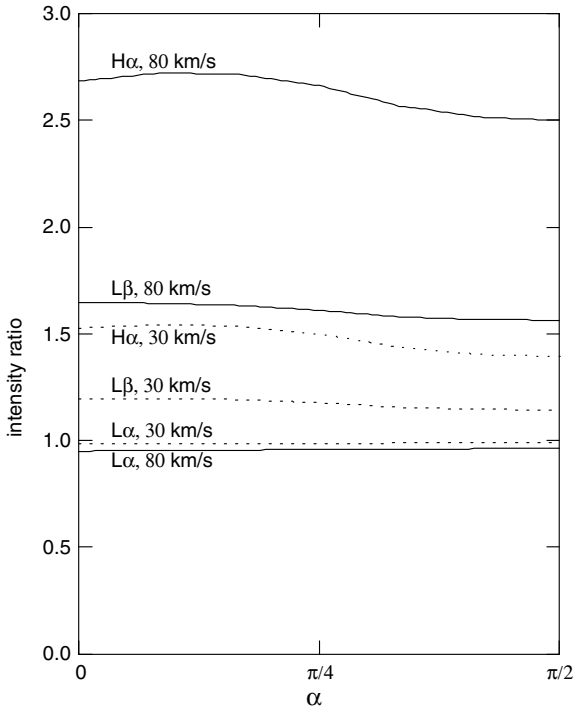

Fig. 10. Effect of Doppler dimming (Lα) or brightening (Lβ and Hα) produced by a longitudinal velocity V_z = 30 (dotted line) or 80 (full line) km s^{-1}. The ratios of intensities between the dynamic and the static models, for the 3 lines and the two velocities, are plotted vs. the inclination angle α (0 corresponds to the foot of the loop, $\pi/2$ to the top).

velocity fields of any direction, i.e. with radial, tangential, and longitudinal components. This means that it could be used for modeling loop oscillations and flows of matter, with or without rotation. Concerning the applications of the numerical methods described in this series of papers, it is worth noting that the 1D code has been used for modeling the chromospheric fine structure from VAULT data (Patsourakos et al. 2007). The present code could be used either as a diagnostic tool for interpreting observations or as a complement to theoretical (MHD or thermodynamical) modeling. Future investigations should include other atomic species than hydrogen, in order to extend the field of applications.

References

Betta, R., Peres, G., Serio, S., & Orlando, S. 1999, in Magnetic Fields and Solar Processes, ESA SP-448, 475
Chae, J., Wang, H., Qiu, J., Goode, P. R., & Wilhelm, K. 2000, ApJ, 533, 535
Doyle, J. G., Taroyan, Y., Ishak, B., Madjarska, M. S., & Bradshaw, S. J. 2006, A&A, 452, 1075
Gontikakis, C., Vial, J.-C., & Gouttebroze, P. 1997a, A&A, 325, 803
Gontikakis, C., Vial, J.-C., & Gouttebroze, P. 1997b, Sol. Phys. 172, 189
Gouttebroze, P. 2004, A&A, 413, 733 (Paper I)
Gouttebroze, P. 2005, A&A, 434, 1165 (Paper II)
Gouttebroze, P. 2006, A&A, 448, 367 (Paper III)
Heinzel, P., & Rompolt, B. 1987, Sol. Phys. 110, 171
Labrosse, N., Gouttebroze, P., & Vial, J.-C. 2007, A&A, 463, 1171
Legras, J. 1963, Précis d'Analyse Numérique (Paris: Dunod), 124
Olson, G. L., Auer, L. H., & Buchler, J. R. 1986, JQSRT 35, 431
Patsourakos, S., Gouttebroze, P., & Vourlidas, A. 2007, ApJ, 664, 1214
Robb, T. D., & Cally, P. S. 1992, ApJ, 397, 329
Roberts, B. 2002, in Solar Variability: From core to Outer Frontiers, ESA SP-506, 481
Rybicki, G. B., & Hummer, D. G. 1991, A&A, 245, 171
Werner, K., & Husfeld, D. 1985, A&A, 148, 417